




Cite this: *Nanoscale*, 2023, **15**, 17946

Hollow spherical $\text{Mn}_{0.5}\text{Zn}_{0.5}\text{Fe}_2\text{O}_4$ nanoparticles with a magnetic vortex configuration for enhanced magnetic hyperthermia efficacy†

Kaiming Shen,^a Lixian Li,^{*b} Funan Tan,^c Shuo Wu,^c Tianli Jin,^c Jingxiang You,^a Mun Yin Chee,^c Yunfei Yan ^{*a} and Wen Siang Lew^{*c}

Conventional magnetic nanoagents in cancer hyperthermia therapy suffer from a low magnetic heating efficiency. To address this issue, researchers have pursued magnetic nanoparticles with topological magnetic domain structures, such as the vortex-domain structure, to enhance the magnetic heating performance of conventional nanoparticles while maintaining excellent biocompatibility. In this study, we synthesized hollow spherical $\text{Mn}_{0.5}\text{Zn}_{0.5}\text{Fe}_2\text{O}_4$ (MZF-HS) nanoparticles using a straightforward solvothermal method, yielding samples with an average outer diameter of approximately 350 nm and an average inner diameter of about 220 nm. The heating efficiency of the nanoparticles was experimentally verified, and the specific absorption rate (SAR) value of the hollow MZF was found to be approximately 1.5 times that of solid MZF. The enhanced heating performance is attributed to the vortex states in the hollow MZF structure as validated with micromagnetic simulation studies. *In vitro* studies demonstrated the lower cell viability of breast cancer cells (MCF-7, BT549, and 4T1) after MHT in the presence of MZF-HS. The synthesized MZF caused 51% cell death after MHT, while samples of MZF-HS resulted in 77% cell death. Our findings reveal that magnetic particles with a vortex state demonstrate superior heating efficiency, highlighting the potential of hollow spherical particles as effective heat generators for MHT applications.

Received 27th July 2023,
 Accepted 12th October 2023

DOI: 10.1039/d3nr03655c

rsc.li/nanoscale

1. Introduction

Magnetic hyperthermia therapy (MHT) is a medical treatment technique that uses magnetic nanoparticles (MNPs) to generate heat and destroy cancer cells.^{1–4} In MHT, magnetic nanoparticles absorb energy from an alternating magnetic field (AMF) and convert it into heat, which can be used to kill cancer cells. MHT has the potential to be a less invasive and more targeted treatment for cancer than traditional treatments like chemotherapy or radiation therapy. To achieve the desired effect there is a need to overcome the major obstacle of developing magnetic nanoparticles with a high specific absorption rate (SAR) which operates within a safe tolerance field.^{5,6} Previous studies have focused on the optimization of single-domain magnetic nanoparticle properties, such as by tuning the shape, size, composition, and magnetic anisotropy to

enhance their efficiency in MHT.^{7–9} The improved magnetic properties of ferrimagnetic iron oxide nanoparticles have resulted in a significant improvement of SAR values, increasing them from approximately ~ 10 to $\sim 1000 \text{ W g}^{-1}$.¹⁰ Further enhancement has also been achieved *via* exchange-coupling^{11,12} and improvement of magneto-crystalline anisotropy.^{13,14} Ferrimagnetic iron oxide nanoparticles possess a certain remanence and stray field, which leads to inevitable agglomeration due to the magnetic dipole–dipole interaction.^{15,16} Recently, MNPs possessing a magnetic vortex ground state have emerged as highly promising biomedical materials, owing to their significantly higher saturation magnetization in comparison to conventional superparamagnetic nanoparticles.^{17–21} The flux-closure structure of the vortex configuration leads to an enhanced heating efficiency, even at a lower concentration and under a safer magnetic field. Additionally, the unique magnetic vortex structure endows the MNPs with great colloidal stability due to negligible remanent magnetization and the absence of a stray field. The vortex nanoring,^{19–22} nanodisc,²³ cubic²⁴ and ellipsoid²⁵ structures with high saturation magnetization have been reported to show high MHT efficiency. Furthermore, Wong *et al.*^{26,27} demonstrated a substantial fourfold increase in heating efficiency, which was attributed to the formation of multiple vortices as opposed to a single vortex configuration. The utiliz-

^aKey Laboratory of Low-grade Energy Utilization Technologies and Systems, Chongqing University, Chongqing 400044, China. E-mail: yunfeiyan@cqu.edu.cn

^bDepartment of Pharmacy, Chongqing University Cancer Hospital, Chongqing 400030, China. E-mail: lilixian@cqu.edu.cn

^cSchool of Physical and Mathematical Sciences, Nanyang Technological University, 21 Nanyang Link, Singapore 637371, Singapore. E-mail: wensiang@ntu.edu.sg

† Electronic supplementary information (ESI) available. See DOI: <https://doi.org/10.1039/d3nr03655c>

ation of magnetic nanoparticles featuring a multi-vortex structure presents a promising way towards achieving even greater advancements in the heating efficiency.

Nanoparticles exhibiting a hollow morphology have garnered growing research interest due to their substantial pore volume, elevated surface-to-volume ratio, and reduced density in comparison to solid nanoparticles of similar dimensions.^{28–30} For example, hollow nanoparticles can serve as high-performance targeted drug carriers due to the hollow nature of the MNPs.^{31–33} Additionally, micromagnetic simulations were conducted on hollow spherical particles, revealing that the presence of a stable vortex state is dependent on the critical particle size. Particularly, as the shell thickness decreases, the critical particle size decreases further, indicating the influence of the shell thickness on the stability of the vortex state.¹⁷ To elucidate the underlying mechanism behind the MHT resulting from the magnetic vortex configuration, it is indispensable to explore its inhibitory effect on cancer cells by a combination of experimental and simulation methods. In this study, we have synthesized spherical $\text{Mn}_{0.5}\text{Zn}_{0.5}\text{Fe}_2\text{O}_4$ (MZF) and hollow $\text{Mn}_{0.5}\text{Zn}_{0.5}\text{Fe}_2\text{O}_4$ (MZF-HS) to investigate their structural effects on MHT properties. Micromagnetic simulation was utilized to explore the magnetization vortex configurations and reversal behaviors. Finally, the MHT performance of MZF-HS was evaluated in MCF-7, BT549, and 4T1 cells under AMF for 10 min.

2. Materials and methods

2.1. Synthesis of hollow spherical $\text{Mn}_{0.5}\text{Zn}_{0.5}\text{Fe}_2\text{O}_4$ -PEG

The synthesis procedure of the hollow spherical $\text{Mn}_{0.5}\text{Zn}_{0.5}\text{Fe}_2\text{O}_4$ -PEG is as follows: first, $\text{FeCl}_3 \cdot 6\text{H}_2\text{O}$ (1.08 g), ZnCl_2 (0.13 g), and $\text{MnCl}_2 \cdot 4\text{H}_2\text{O}$ (0.198 g) were dissolved in

60 mL ethylene glycol (EG) under magnetic stirring until a homogenous liquid was obtained. Then, the different amounts of urea (1.45 g, 24 mmol; 1.92 g, 32 mmol; 2.4 g, 40 mmol) and cetyltrimethylammonium bromide (CTAB) (2.18 g, 6 mmol) were added and stirred for 15 min at 90 °C until it became completely transparent. Next, the mixture was transferred into a Teflon autoclave for the solvothermal process and heated at different temperatures (180 °C, 200 °C, 220 °C) for 24 h. After cooling to room temperature, the resulting black solution was washed multiple times with ethanol and deionized water before being dried overnight at 60 °C under vacuum conditions. Finally, CTAB was removed by acetone reflux at 85 °C to obtain pure hollow spherical $\text{Mn}_{0.5}\text{Zn}_{0.5}\text{Fe}_2\text{O}_4$. The synthesis route as shown in Fig. 1.

2.2. Synthesis of hollow spherical $\text{Mn}_{0.5}\text{Zn}_{0.5}\text{Fe}_2\text{O}_4$ -PEG

The as-prepared hollow spherical $\text{Mn}_{0.5}\text{Zn}_{0.5}\text{Fe}_2\text{O}_4$ nanoparticles were modified with PEG-bis-amine. Briefly, 15 mg $\text{Mn}_{0.5}\text{Zn}_{0.5}\text{Fe}_2\text{O}_4$ nanoparticles were ultrasonically dispersed into 20 mL deionized water, then incubated with 250 μL of 100 mg mL^{-1} *N*-ethyl-*N'*-(3-(dimethylamino)-propyl) carbodiimide hydrochloride (EDC) and 200 μL of 100 mg mL^{-1} *N*-hydroxysuccinimide (NHS), and stirred vigorously for 30 min at room temperature. Subsequently, the resulting NHS-activated nanoparticles were covalently linked to NH_2 -PEG- NH_2 (300 μL 100 mg mL^{-1}) at room temperature by stirring for 6 h, and then dried at 60 °C in a vacuum for 12 h.

2.3. Magnetothermal measurements in aqueous suspension

An AMF with an amplitude of 6.7 kA m^{-1} at a fixed frequency of 300 kHz was applied to induce MHT. Time-dependent temperature curves of $\text{Mn}_{0.5}\text{Zn}_{0.5}\text{Fe}_2\text{O}_4$ -PEG aqueous solution were obtained by the calorimetric method and different concentrations of $\text{Mn}_{0.5}\text{Zn}_{0.5}\text{Fe}_2\text{O}_4$ -PEG aqueous solution in EP tubes

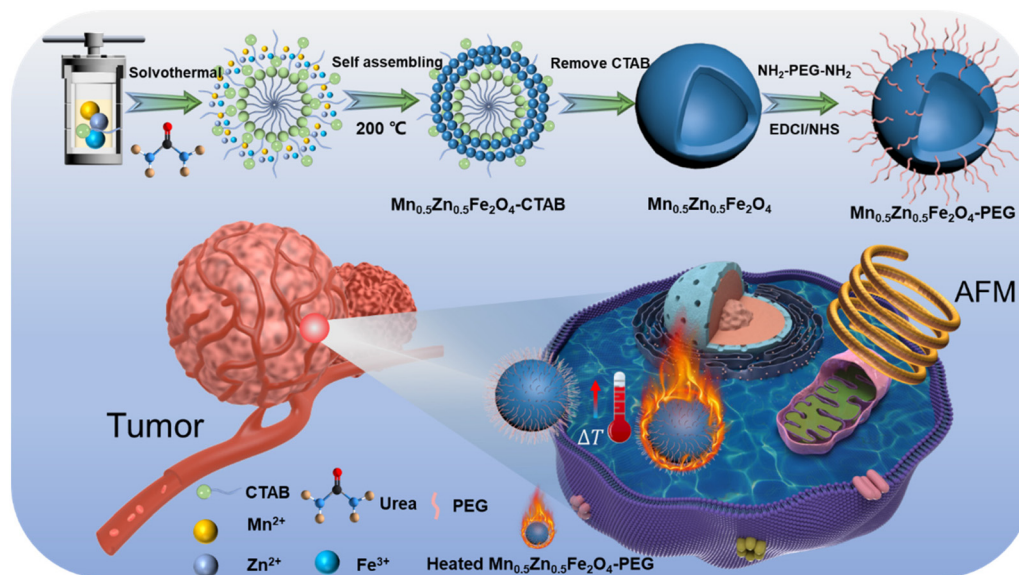


Fig. 1 Illustration of the synthesis process of MZF-HS-PEG and the schematic diagram for MHT.

(3 mL) were placed within the magnetic coils. To quantitatively assess the heating efficiency, the specific absorption rate (SAR), which quantifies the amount of energy converted into heat per unit time and mass, was calculated with the following eqn (1):³⁴

$$\text{SAR} = C \left(\frac{dT}{dt} \right) \left(\frac{m_s}{m_m} \right) \quad (1)$$

where C is the specific heat capacity of water (4.18 J g K^{-1}), $\frac{dT}{dt}$ is the initial slope of the time-dependent temperature curve, m_s is the mass of the suspension and m_m is the mass of $\text{Mn}_{0.5}\text{Zn}_{0.5}\text{Fe}_2\text{O}_4\text{-PEG}$.

2.4. Micromagnetic simulations

The magnetization configuration of the hollow spherical $\text{Mn}_{0.5}\text{Zn}_{0.5}\text{Fe}_2\text{O}_4$ (MZF-HS) nanoparticles was investigated using MuMax3 to solve the Landau–Lifshitz–Gilbert (LLG) eqn (2) in three dimensions.²⁷

$$\frac{\partial M(r, t)}{\partial t} = \gamma_G (M(r, t) \times H_{\text{eff}}) - \frac{\alpha_G}{M_s} M(r, t) \times H_{\text{eff}} \quad (2)$$

where $M(r, t)$ is the magnetization vector, H_{eff} is the effective field, M_s is the saturation magnetization, γ_G is the gyromagnetic ratio ($1.78 \times 10^7 \text{ s}^{-1} \text{ Oe}^{-1}$), and α_G is the damping coefficient.

The micromagnetic simulations yielded valuable insights into the magnetization configurations and reversal behaviors of MZF-HS at the microscopic level, establishing a correlation between theoretical models and observations derived from experimental results. The system's total energy encompasses four components: exchange energy (E_{Exchange}), Zeeman energy (E_{Zeeman}), anisotropy energy ($E_{\text{Anisotropy}}$), and demagnetizing energy (E_{Demag}) as shown in the eqn (3).

$$E_{\text{Total}} = E_{\text{Exchange}} + E_{\text{Zeeman}} + E_{\text{Anisotropy}} + E_{\text{Demag}}. \quad (3)$$

The materials parameters for $\text{Mn}_{0.5}\text{Zn}_{0.5}\text{Fe}_2\text{O}_4$ were employed in the simulation and are as follows: M_s of $400 \times 10^3 \text{ A m}^{-1}$, exchange stiffness constant A_{ex} of $1.2 \times 10^{-11} \text{ J m}^{-1}$, magneto-crystalline anisotropy $k = 0$, and the Gilbert damping constant α of 0.1. A cell size of $4 \text{ nm} \times 4 \text{ nm} \times 4 \text{ nm}$ was applied for all the simulations.

3. Results and discussion

3.1. Structure and magnetism

Transmission electron microscopy (TEM) imaging was employed to investigate the morphology of the hollow spherical $\text{Mn}_{0.5}\text{Zn}_{0.5}\text{Fe}_2\text{O}_4$ nanoparticles. As shown in Fig. 2a–c, no hollow spherical structure is formed when the molar ratio between urea and iron is 1 : 6. However, an obvious hollow spherical $\text{Mn}_{0.5}\text{Zn}_{0.5}\text{Fe}_2\text{O}_4$ morphology is found when the molar ratio is 1 : 8 and 1 : 10, and the average nanoparticle diameter of the hollow spherical samples is about 350 nm, their size distribution conforms to Sturges' criterion,³⁵ as shown in

Fig. 2f; the average inner diameter size is about 220 nm as displayed in Fig. 2h. In the reaction process, urea (H_2NCONH_2) provides an alkaline environment and releases NH_3 to produce a hollow structure; the reaction mechanism is presented in the ESI (Fig. S3†). When the content of urea increases to 32 mmol, the MZF spheroid has the best morphology and a clear spheroid boundary, as shown in Fig. S1a and b.† When the urea content was increased further, the spheres became more irregular and began to break up, as shown in Fig. S1c.† The damage degree can be reduced by controlling the amount of urea reasonably. Additionally, the nanoparticles have a good dispersion due to the low stray field and the modified surface of the hollow spherical nanoparticles with PEG. The scanning electron microscopy (SEM) images of the sample indicate the hollow nature of spherical $\text{Mn}_{0.5}\text{Zn}_{0.5}\text{Fe}_2\text{O}_4$, as depicted in Fig. 2d and e, and the SEM images of $\text{Mn}_{0.5}\text{Zn}_{0.5}\text{Fe}_2\text{O}_4$ when the molar ratio is 1 : 10 are depicted in Fig. S2.† The EDS mapping is shown in Fig. 2g which indicates that Mn, Zn, Fe, and O are homogeneously distributed in the obtained MZF-HS. Room-temperature hysteresis loops were examined to analyze the magnetic features of $\text{Mn}_{0.5}\text{Zn}_{0.5}\text{Fe}_2\text{O}_4$ nanoparticles. M_s exhibits an increasing trend with a higher molar ratio between urea and iron, reaching its maximum value of 61.3 emu g^{-1} at a molar ratio of 1 : 10, as depicted in Fig. 2i. The results suggest that M_s is related to the structure of the magnetic nanoparticles.

Da Silva *et al.*^{36,37} prepared cubic spinel ferrite-based nanoparticles by precisely regulating the molar ratio of different metals and studied the influence of different stoichiometric ratios on its magnetic properties. In this study, we are committed to the comparative study of the effect of the hollow structure on its magnetothermal properties, and only a single stoichiometric ratio sample is prepared, which can be seen from the XRD pattern that it is a pure spinel structure. The X-ray diffraction (XRD) data are presented in Fig. 3a; it is confirmed from the XPS spectra that $\text{Mn}_{0.5}\text{Zn}_{0.5}\text{Fe}_2\text{O}_4$ was successfully synthesized, and XRD can also confirm this by comparing the standard PDF peaks of the MnZn ferrite (JCPDS no. 74-2403).³⁸ $2\theta \approx 18.7^\circ, 29.98^\circ, 35.71^\circ, 42.35^\circ, 53.27^\circ, 57.27^\circ, 62.36^\circ, 74.24^\circ$ and 88.6° are the obvious diffraction peaks, corresponding to the cubic spinel ferrite diffraction peaks of the (200), (220), (311), (222), (400), (422), (511), (440), (533) and (415) crystal faces.

As shown in Fig. 3b, the Fe2p peaks comprise two primary asymmetric peaks, namely Fe2p_{3/2} and Fe2p_{1/2}, exhibiting binding energies of 710.5 eV and 723.8 eV, respectively. The two minor peaks observed at approximately 718.8 eV and 731 eV correspond to the satellite peaks of Fe2p_{3/2} and Fe2p_{1/2}, respectively. The findings indicate that Fe³⁺ is the sole oxidation state observed on the MZF-NFL surface/near-surface. Regarding the Fe2p_{3/2} peak, the presence of three distinct contributions at approximately 709.8 eV, 711 eV, and 712.3 eV corresponds to three distinct bonding states of Fe³⁺ ions. The peaks observed at 709.8 eV and 711 eV can be attributed to the Fe³⁺ cations with varying occupancies (either tetrahedral or octahedral) within the spinel ferrite structure. Conversely, the

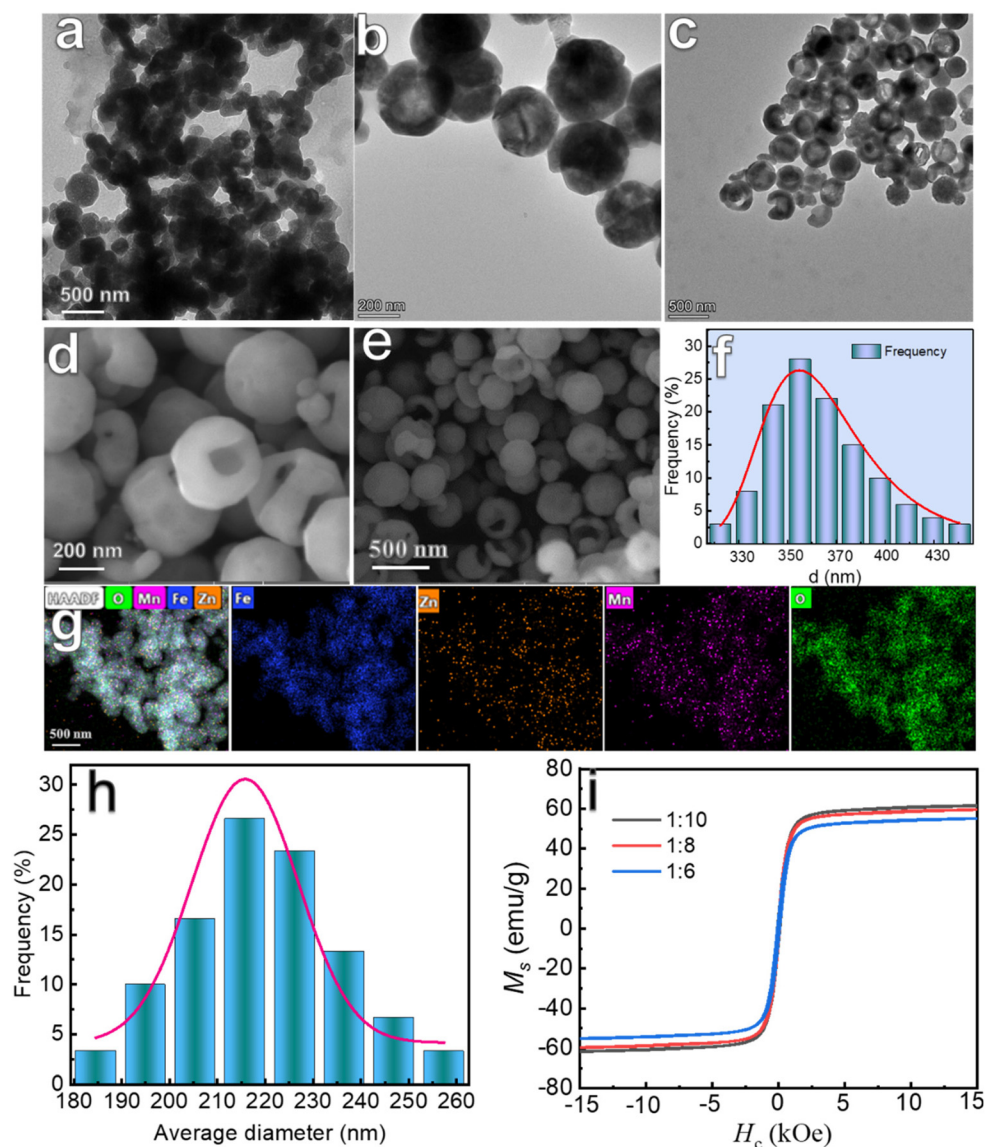


Fig. 2 The TEM images of (a) MZF, (b) MZF-HS (1 : 8), and (c) MZF-HS (1 : 8). The SEM images of (d) MZF, and (e) MZF-HS (1 : 8). (f) the size distribution of MZF-HS. (g) TEM-EDS elemental mapping images of individual MZF nanoparticles. (h) The average inner size distribution of MZF-HS. (i) The H - M curves of MZF.

peak at a higher binding energy of approximately 712.3 eV corresponds to Fe^{3+} ions bonded with hydroxyl groups.³⁹ In the high-resolution XPS of $\text{Mn}2\text{p}$, the corresponding $\text{Mn}2\text{p}_{1/2}$ and $\text{Mn}2\text{p}_{3/2}$ signals are observed at 653 and 643.8 eV in a $\sim 2 : 1$ peak area ratio marking that Mn is present in a +2 oxidation state (Fig. 3c). Fig. 3d presents the XPS spectrum of $\text{Zn}2\text{p}$, revealing the presence of the Zn oxidation state through the two peaks observed at 1021.6 eV and 1044.6 eV.⁴⁰

Exploring the application of the as-prepared MZF-HS in tumor hyperthermia therapy, the magnetothermal experiment system is shown in Fig. S4.† Fig. 4a illustrates the magnetic induction heating process. The SAR of MZF and MZF-HS, with concentrations ranging from 1 to 7 mg mL^{-1} , were employed to assess their heat generation capacities when exposed to an

AMF ($H = 6.7 \text{ kA m}^{-1}$, $f = 300 \text{ kHz}$) for a duration of 10 min. Temperature elevation has a strong dependence on the concentration of magnetic nanoparticles, as shown in Fig. 4b and c; the experimental data were fitted using the Box-Lucas model⁴¹ to obtain the typical heat transfer time and the asymptotic temperature. And more details are provided in Fig. S5.† Additionally, the typical heat transfer time and the asymptotic temperature are listed in Table S1.† As shown in Fig. 4d, the MZF magnetic inductive heating capacity is obviously lower than MZF-HS. The SAR value of MZF-HS is close to 1.5 times of MZF at a concentration of 1.0 mg mL^{-1} . Furthermore, the magnetic field strength is also another important factor affecting magnetic induction heating. As shown in Fig. 4e and f, the magnetic heating rate increases sig-

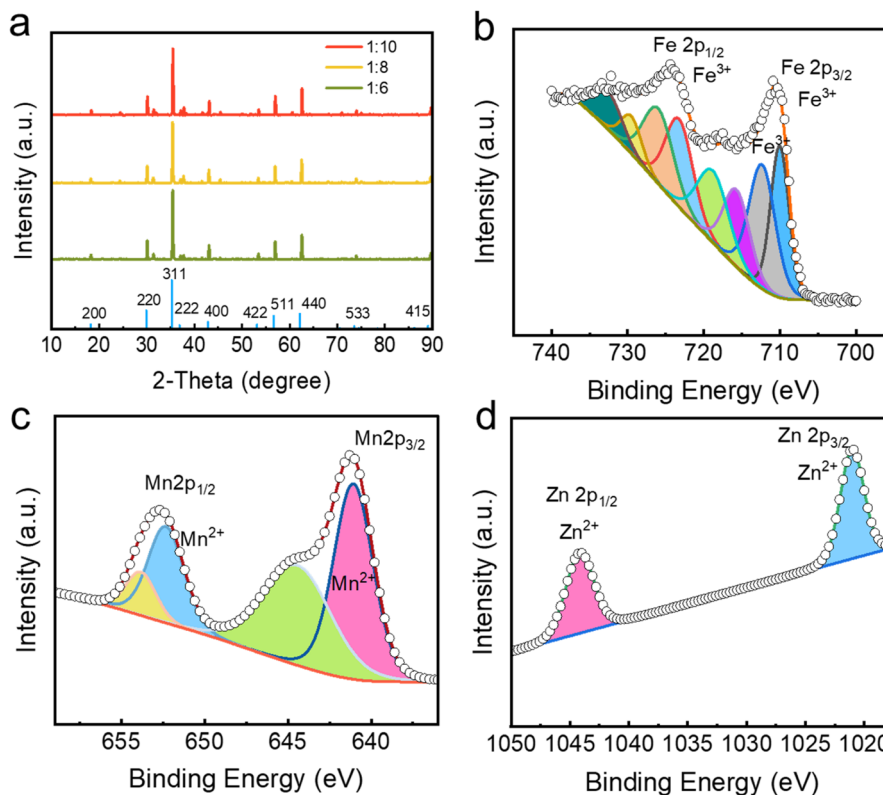


Fig. 3 (a) XRD patterns of MZF-HS. High-resolution XPS spectra of (b) Fe2p, (c) Mn2p, and (d) Zn2p.

nificantly with the increase of H . The temperature difference of MZH-HS solutions under various H can be observed from the infrared thermal image in Fig. 4g. As shown in Fig. 4h, with the increase of magnetic field strength, the SAR value increases significantly.

In the previous study, the magnetic vortex configuration for hollow spherical particles has been confirmed by the experimental method.¹⁷ To investigate the difference in the SAR of MZF and MZF-HS, the magnetization dynamics were studied using micromagnetic simulation. A two-dimensional cross-section of the simulation model with different ϵ values is shown in Fig. 5a, where $\epsilon = \frac{\text{inner radius}}{\text{external radius}}$. The external radius was maintained at 350 nm, while the inner radius was varied. The ϵ value of the as-prepared MZF-HS in this work is about 0.7, as shown in Fig. 2c. Hysteresis loops were obtained by varying ϵ from 0 to 0.9; the sweep magnetic field magnitude spans from -2 k Oe to $+2\text{ k Oe}$. Fig. 5b–e illustrate the normalized hysteresis loops of MZF-HS at $\epsilon = 0, 0.5, 0.7$ and 0.9 , respectively. The details for $\epsilon = 0.1$ and 0.3 are presented in Fig. S6a and b.† The hysteresis loop area within ± 100 Oe is significantly larger at $\epsilon = 0.7$ and 0.9 , indicating enhanced heating performance as observed experimentally. As depicted in Fig. 5b, a single domain state was observed at point A, and this state persists until point B. At this stage, the field is gradually lowered, overcoming the energy barrier and leading to the gradual formation of a vortex state corresponding to point C,

and magnetic state transitions were observed as the differential magnetic susceptibility, $\chi = dM/dH$ decreased as shown in Fig. 5f. On further reduction of H to -1500 Oe (point D), the magnetization configuration saturates into a single domain state. Additionally, for values of ϵ less than 0.5, the magnetization reversal behaviors are similar to those for $\epsilon = 0.5$ (Fig. S6a and b.†). With an increase in ϵ to above 0.5, a higher frequency of magnetic state transitions is observed, indicated by the occurrence of multiple abrupt magnetization switching resulting in an increased number of spikes in χ , as depicted in Fig. 5g–i. The χ details for $\epsilon = 0.1$ and 0.3 are presented in Fig. S6c and d.† As the magnetic field is swept from negative to positive, the magnetization configuration undergoes a transition from a negative single-domain state to a positive single-domain state, as illustrated in Fig. 6a. Specifically, at $H = -600$ Oe, a distinctive double vortex state emerges, consisting of a pair of clockwise and counterclockwise vortices. Separated by a domain wall, the two vortices possess their vortex axis parallel to the magnetic field, while the spins of the domain wall align themselves along the magnetic field direction, as depicted in Fig. 6b. This domain wall narrows with the lowering of the magnetic field which extends the vortex region. Upon further reduction of the magnetic field to -300 Oe, the magnetic structure transitions into a single vortex configuration. The single magnetic vortex state is maintained until the reverse magnetic field is increased to $+1500$ Oe before saturating into

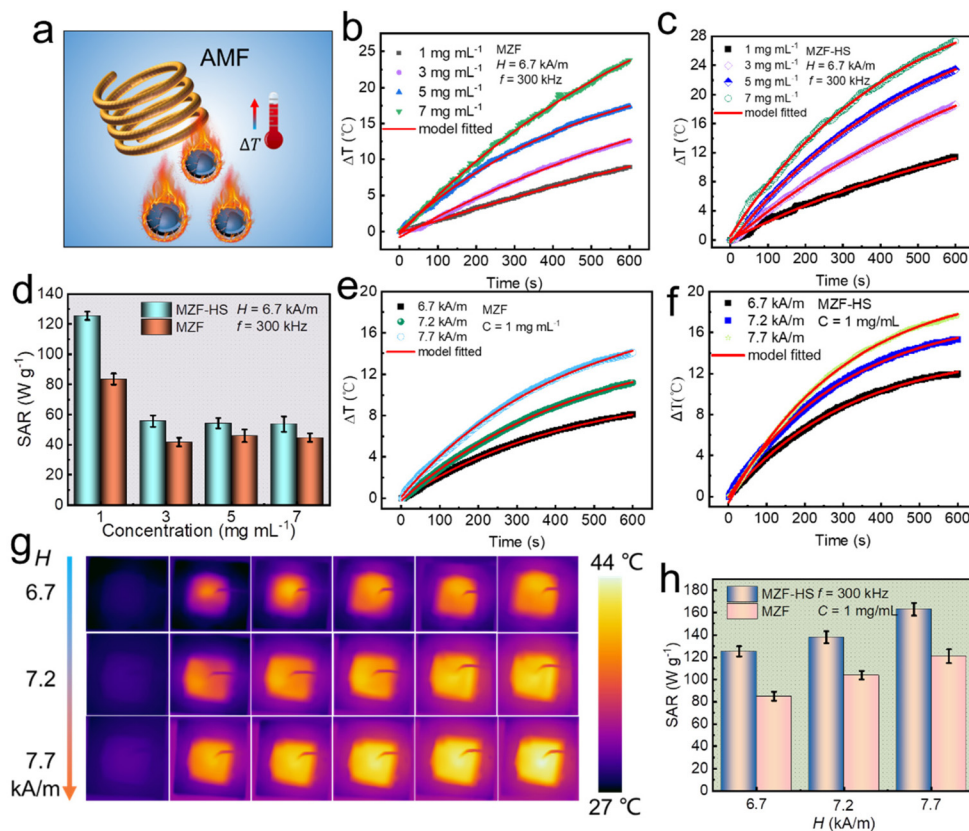


Fig. 4 (a) Magnetic induction heating diagram. Temperature–time curves of MZF-HS, with $\varepsilon = 0$ (b) and $\varepsilon = 0.7$ (c), for increasing the concentration of MZF-HS from 1 to 7 mg mL^{-1} , the experimental data are represented by filled symbols and the fitting data are represented by solid red lines. (d) The SAR values of MZF ($\varepsilon = 0$) and MZF-HS ($\varepsilon = 0.7$) under different concentrations. Temperature–time curves of MZF-HS, (e) with $\varepsilon = 0$, and (f) $\varepsilon = 0.7$ on increasing H from 6.7 to 7.7 kA m^{-1} . (g) Infrared thermal images of MZF-HS ($\varepsilon = 0.7$, $C = 1 \text{ mg L}^{-1}$) under different H excitations. (h) SAR values of MZF ($\varepsilon = 0$) and MZF-HS ($\varepsilon = 0.7$) under various H excitations.

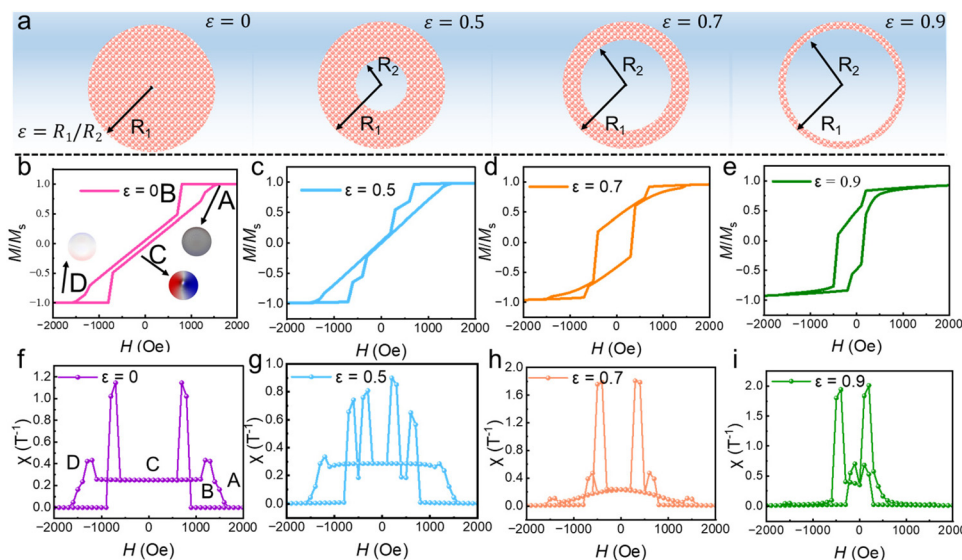


Fig. 5 (a) A 2D schematic diagram of different ε MZF-HS. The simulated normalized hysteresis loops of MZF-HS with $\varepsilon = 0$ (b), $\varepsilon = 0.5$ (c), $\varepsilon = 0.7$ (d), and $\varepsilon = 0.9$ (e). The differential magnetic susceptibility χ ($\chi = dM/dH$) of MZF-HS with different inner/external radius ratios (ε) and the normalized hysteresis loops of MZF-HS with $\varepsilon = 0$ (f), $\varepsilon = 0.5$ (g), $\varepsilon = 0.7$ (h), and $\varepsilon = 0.9$ (i).

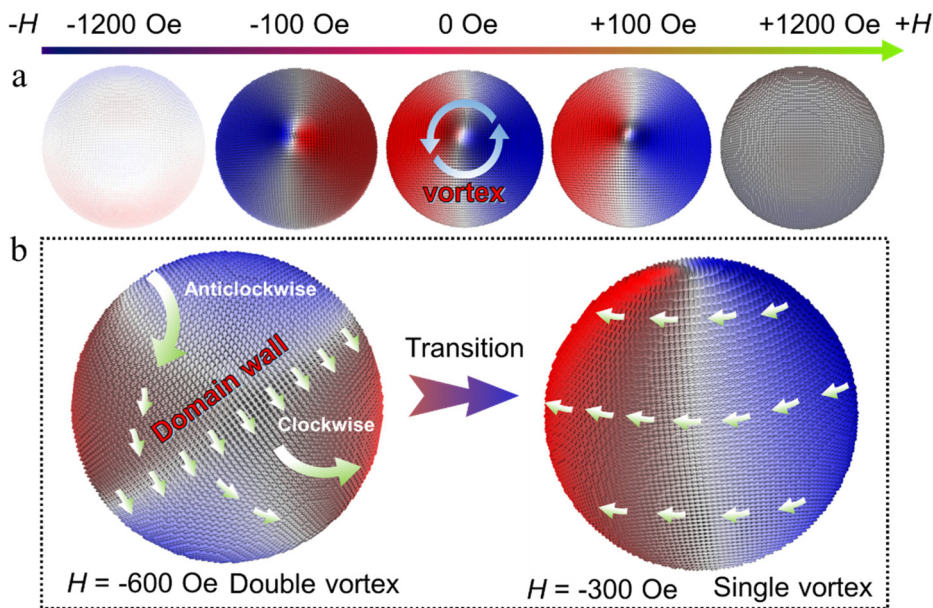


Fig. 6 (a) The magnetization configuration for MZF-HS with $\epsilon = 0.7$ under an external field sweep. (b) The field-induced double vortex comprising a pair of transitions of counterclockwise and clockwise vortices into a single vortex state.

a single domain state. The formation of stable double vortex states is observed across a wide range of ϵ values, particularly when ϵ exceeds 0.5. This behavior can be attributed to the diminishing contribution of the demagnetization field, energetically favoring the formation of a domain wall. Conversely, for ϵ values below 0.5, there is a higher contribution from the demagnetization field, resulting in only a single vortex state. Hence, the presence of a hollow structure plays a crucial role in stabilizing the double vortex configuration. It is worth noting that according to the study of Aquino *et al.*,⁴² the opening of the hysteresis cycle is observed on both sides of the center of the hysteresis loop, while in this experiment, no obvious opening was found on both sides of the center of the hysteresis loop measured. Indeed, the measured hysteresis loop is the sum of the interactions of many nanoparticles, such as the dipole interaction, which affects the hysteresis loop, so that the loop cannot match the loop of a single particle.

In addition to analyzing the magnetization structure, we present the variations of exchange energy, demagnetization energy, Zeeman energy, and total energy as a function of the external magnetic field H , as illustrated in Fig. 7a–d, respectively. For clarity, the exchange energy curves for $\epsilon = 0.1, 0.3, 0.7$, and 0.9 are depicted in Fig. S7a and b† separately. As the magnetic field undergoes reversal, the exchange energy experiences sharp drops, for $\epsilon = 0$, the drop indicates the formation of a single domain from a vortex state, while multiple drops for $\epsilon = 0.5$ signify the state change from a double vortex to a single vortex before saturating at a single domain state. For ϵ values exceeding 0.5, the pair of counterclockwise and clockwise vortex cores results from the interplay between magnetostatic energy and exchange energy. In the presence of a strong magnetic

field, the dominant contribution to the total magnetic energy arises from the Zeeman energy. Consequently, the spins predominantly align along the direction of the magnetic field, effectively minimizing the impact of the exchange energy on the overall magnetic energy. With the reduction of the applied magnetic field, the demagnetization effects and stray fields are minimized. As depicted in Fig. 7d, with the increase of ϵ , the vortex states are more stable as indicated by the lower total energy in the system. At sufficiently low magnetic fields, the reduction in shell thickness results in the formation of a stable double vortex state. The existence of stable vortices in MZF-HS suggests that the vortices contribute to the improved SAR observed experimentally.

Although MZF has been shown to have good cytocompatibility in previous studies,⁴³ particle size also has a significant impact on cytotoxicity.⁴⁴ Therefore, the cytotoxicity of MZF-HS was first evaluated for MCF-7 cells with the methyl thiazolyltetrazolium (MTT) assay. The dose dependence of cell viability is curve-fitted using Hill's equation according to a method reported by Li *et al.*,⁴⁵ as shown in Fig. S8.† The cooperativity index is $\gamma = 0.53$ for the control group conditions (MCF-7 cells incubated with MZF-HS under dark conditions), the finding indicates positive cooperativity for the control group conditions. As shown in Fig. 8a, after incubation for 24 h and 48 h, MZF-HS exhibits no remarkable cytotoxicity against MCF-7 cells as evidenced by the cell viability of more than 80%, even at a high concentration of $200 \mu\text{g mL}^{-1}$, indicating the favorable biosafety of MZF-HS. The cell cytotoxicity was also evaluated in the MCF-7, BT549 and 4T1 cells under the AMF. As expected, the AMF ($f = 300 \text{ kHz}$, $H = 6.7 \text{ kA m}^{-1}$) enhances the cell ablation. Fig. 8b illustrates the results of cell

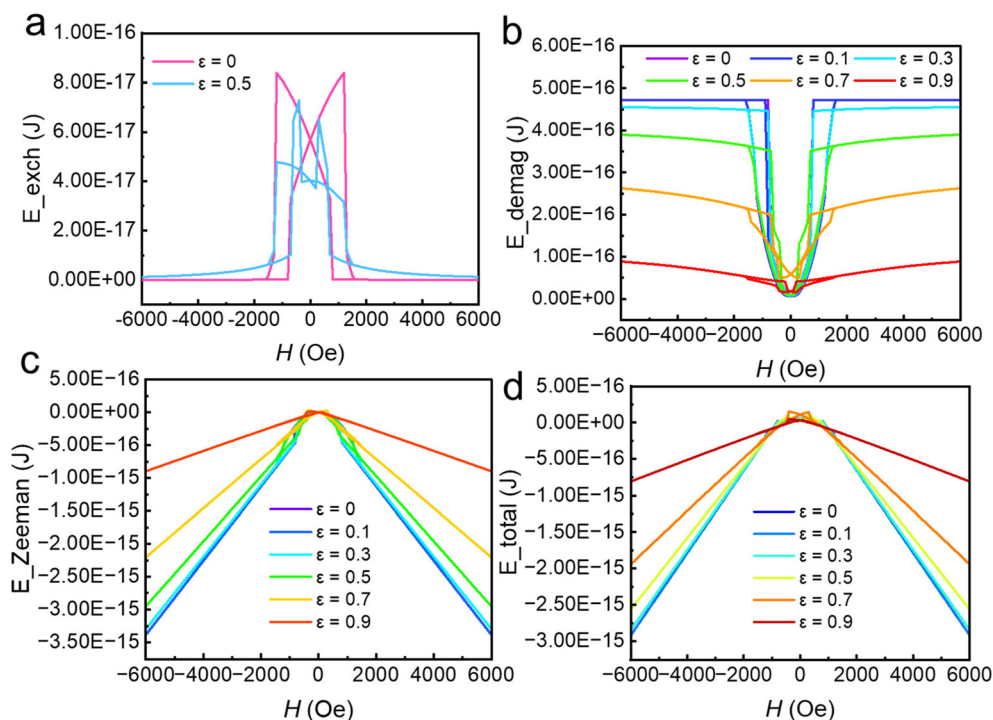


Fig. 7 The curves of (a) E_{exch} , (b) E_{demag} , (c) E_{Zeem} , and (d) E_{total} as a function of magnetic field H .

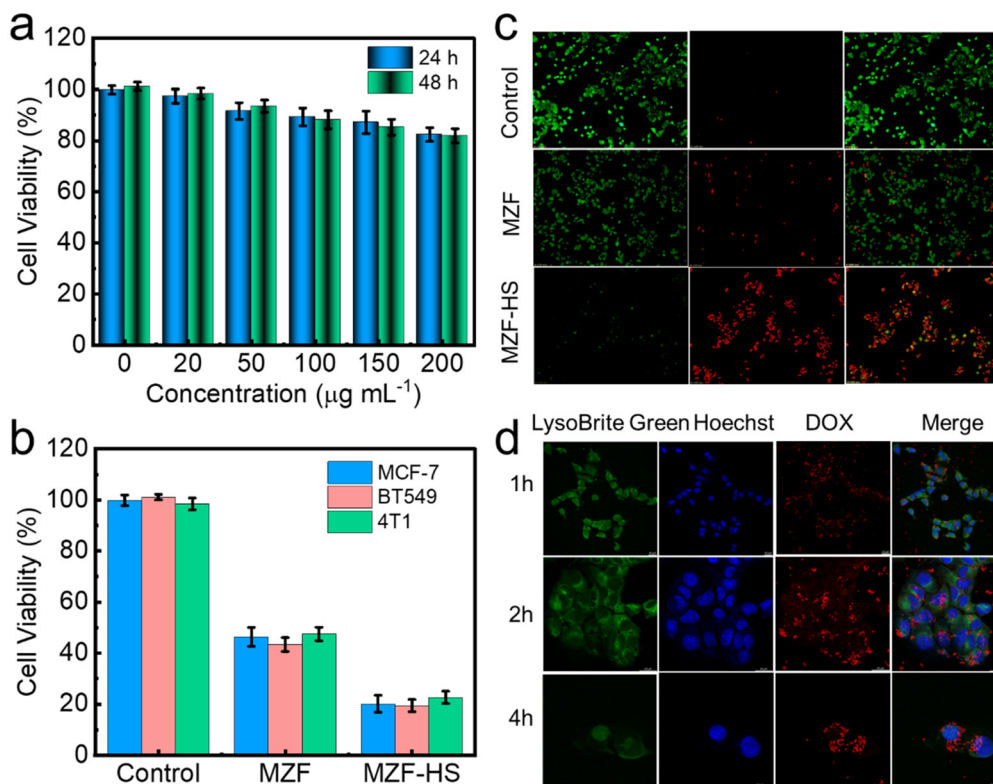


Fig. 8 (a) MCF-7 cells incubated with different concentrations of MZF-HS for 24 h and 48 h. (b) The viability of MCF-7, BT549 and 4T1 cells was assessed upon incubation with MZF-HS and exposure to an AMF with a frequency of 300 kHz and a magnetic field strength of 7.0 kA m^{-1} for a duration of 10 min. (c) The confocal images depict calcein-AM (green, live cells) and propidium iodide (red, dead cells) staining of cells that were incubated with MZF-HS (1 mg mL^{-1}) and subjected to treatment with an AMF with a frequency of 300 kHz and a magnetic field strength of 7.0 kA m^{-1} for a duration of 10 min. (d) Confocal microscope images of the cellular uptake of MZF-HS in MCF-7 cells after 1 h, 2 h, and 4 h.

viability upon exposure to AMF ($f = 300$ kHz, $H = 6.7$ kA m⁻¹). At a concentration of 1.0 mg mL⁻¹, the cell death maintains at a level of <55% for MZF, while a marked increase in the cell death of >77% for MZF-HS was observed. Furthermore, a fluorescent LIVE/DEAD assay was also performed to visualize the cell viability (Fig. 8c). Almost no dead cells in the control group were observed. Approximately 51% of the cells died in the MZF group, whereas more than 77% of the cells died in the MZF-HS group. These results are consistent with the SAR results and corroborate with the simulation findings, demonstrating that MZF-HS has an excellent hyperthermia effect at the cellular level.

Additionally, the uptake behavior of MZF-HS was tracked using confocal laser scanning microscopy to capture fluorescence images. The cell nuclei were stained with Hoechst, which emits blue fluorescence upon illumination with a 405 nm laser. Under excitation from a 488 nm laser, the MZF-HS/DOX complex exhibited red fluorescence. In contrast, the lysosome was stained with Lysobrite green and displayed green fluorescence upon illumination at 500 nm. As depicted in Fig. 8d, MCF-7 cells incubated with MZF-HS/DOX exhibited clear red fluorescence signals within the lysosome, exhibiting colocalization with Lysobrite green. This observation strongly suggests that MZF-HS/DOX was internalized into MCF-7 cells *via* an endolysosomal pathway. The results showed the effective uptake of MZF-HS/DOX by cancer cells. Interestingly, the cells incubated with MZF-HS/DOX displayed slightly weaker red fluorescence signals after 1 h. However, only small amounts of MZF-HS/DOX were observed inside the cells, suggesting that the uptake of free DOX small molecules *via* passive transport is the main mechanism.⁴⁶ In contrast, stronger red fluorescence signals and more MZF-HS/DOX were found inside the lysosome after incubation for 4 h. The primary factor is due to the reliance of nanoscale biomaterials on energy-dependent and relatively slower endocytic pathways.⁴⁷

4. Conclusions

In conclusion, MZF-HS and MZF nanoparticles were successfully synthesized. The SAR value of MZF-HS was approximately 1.5 times that of MZF, demonstrating MZF-HS to be a potential MNP for MHT applications. The micromagnetic simulations unveiled a significant enhancement in the stability of the vortex state and an increase in the hysteresis loop area with increased ϵ , indicating an enhanced heating performance as observed experimentally. *In vitro* studies using breast cancer cells (MCF-7) demonstrated significantly lower cell viability after MHT in the presence of MZF-HS. Specifically, MZF resulted in 51% cell death, whereas MZF-HS resulted in 77% cell death. Considering the superior heating efficiency of MZF-HS, the findings in this study highlight the potential of hollow spherical particles as effective heat generators for MHT applications.

Conflicts of interest

There are no conflicts to declare.

Acknowledgements

The authors gratefully acknowledge the financial support from the Fundamental Research Funds for the Central Universities (2019CDYGYB022), and the Natural Science Foundation of Chongqing (cstc2021jcyj-msxmX0448). This study was also supported by the projects of the Chongqing Clinical Pharmacy Key Specialties Construction Project and Young and Middle-aged Leading Talents in Medical of Chongqing Health Commission.

References

- 1 C. R. Kalaiselvan, S. S. Laha, S. B. Somvanshi, T. A. Tabish, N. D. Thorat and N. K. Sahu, *Coord. Chem. Rev.*, 2022, **473**, 214809.
- 2 X. Liu, Y. Zhang, Y. Wang, W. Zhu, G. Li, X. Ma, Y. Zhang, S. Chen, S. Tiwari, K. Shi, S. Zhang, H. M. Fan, Y. X. Zhao and X. J. Liang, *Theranostics*, 2020, **10**, 3793–3815.
- 3 E. Myrovali, N. Maniotis, T. Samaras and M. Angelakeris, *Nanoscale Adv.*, 2020, **2**, 408–416.
- 4 Y. Park, A. A. Demessie, A. Luo, O. R. Taratula, A. S. Moses, P. Do, L. Campos, Y. Jahangiri, C. R. Wyatt, H. A. Albarqi, K. Farsad, O. D. Slayden and O. Taratula, *Small*, 2022, **18**, e2107808.
- 5 S. K. Sharma, N. Shrivastava, F. Rossi, L. D. Tung and N. T. K. Thanh, *Nano Today*, 2019, **29**, 100795.
- 6 K. Shen, Y. Yan, W. Gao, H. Li, W. Chen, Z. He and L. Li, *J. Alloys Compd.*, 2022, **926**, 166806.
- 7 E. Bertuit, E. Benassai, G. Meriguet, J. M. Greneche, B. Baptiste, S. Neveu, C. Wilhelm and A. Abou-Hassan, *ACS Nano*, 2021, **16**, 271–284.
- 8 H. Gavilan, S. K. Avugadda, T. Fernandez-Cabada, N. Soni, M. Cassani, B. T. Mai, R. Chantrell and T. Pellegrino, *Chem. Soc. Rev.*, 2021, **50**, 11614–11667.
- 9 H. Gavilan, K. Simeonidis, E. Myrovali, E. Mazario, O. Chubykalo-Fesenko, R. Chantrell, L. Balcells, M. Angelakeris, M. P. Morales and D. Serantes, *Nanoscale*, 2021, **13**, 15631–15646.
- 10 Z. Hedayatnasab, F. Abnisa and W. M. A. W. Daud, *Mater. Des.*, 2017, **123**, 174–196.
- 11 J. H. Lee, J. T. Jang, J. S. Choi, S. H. Moon, S. H. Noh, J. W. Kim, J. G. Kim, I. S. Kim, K. I. Park and J. Cheon, *Nanotechnol.*, 2011, **6**, 418–422.
- 12 J. Robles, R. Das, M. Glassell, M. H. Phan and H. Srikanth, *AIP Adv.*, 2018, **8**, 056719.
- 13 G. Niraula, J. A. H. Coaquira, G. Zoppellaro, B. M. G. Villar, F. Garcia, A. F. Bakuzis, J. P. F. Longo, M. C. Rodrigues, D. Muraca, A. I. Ayesh, F. S. M. Sinfrônio, A. S. de Menezes, G. F. Goya and S. K. Sharma, *ACS Appl. Nano Mater.*, 2021, **4**, 3148–3158.

- 14 H. Mamiya, H. Fukumoto, J. L. Cuya Huaman, K. Suzuki, H. Miyamura and J. Balachandran, *ACS Nano*, 2020, **14**, 8421–8432.
- 15 L. C. Branquinho, M. S. Carriao, A. S. Costa, N. Zufelato, M. H. Sousa, R. Miotto, R. Ivkov and A. F. Bakuzis, *Sci. Rep.*, 2013, **3**, 2887.
- 16 P. Garcia-Acevedo, M. A. Gonzalez-Gomez, A. Arnosa-Prieto, L. de Castro-Alves, Y. Pineiro and J. Rivas, *Adv. Sci.*, 2023, **10**, 2203397.
- 17 N. Hirano, S. Kobayashi, E. Nomura, M. Chiba, H. Kasai, Z. Akase, T. Akashi, A. Sugawara and H. Shinada, *Appl. Phys. Lett.*, 2021, **119**, 132401.
- 18 M.-K. Kim, J. Sim, J.-H. Lee and S.-K. Kim, *J. Appl. Phys.*, 2019, **125**, 063901.
- 19 G. R. Lewis, J. C. Loudon, R. Tovey, Y. H. Chen, A. P. Roberts, R. J. Harrison, P. A. Midgley and E. Ringe, *Nano Lett.*, 2020, **20**, 7405–7412.
- 20 X. Liu, J. Zheng, W. Sun, X. Zhao, Y. Li, N. Gong, Y. Wang, X. Ma, T. Zhang, L. Y. Zhao, Y. Hou, Z. Wu, Y. Du, H. Fan, J. Tian and X. J. Liang, *ACS Nano*, 2019, **13**, 8811–8825.
- 21 X. L. Liu, Y. Yang, C. T. Ng, L. Y. Zhao, Y. Zhang, B. H. Bay, H. M. Fan and J. Ding, *Adv. Mater.*, 2015, **27**, 1939–1944.
- 22 J. Bao, S. Guo, X. Zu, Y. Zhuang, D. Fan, Y. Zhang, Y. Shi, Z. Ji, J. Cheng and X. Pang, *Front. Bioeng. Biotechnol.*, 2021, **9**, 721617.
- 23 Y. Yang, X. Liu, Y. Lv, T. S. Herng, X. Xu, W. Xia, T. Zhang, J. Fang, W. Xiao and J. Ding, *Adv. Funct. Mater.*, 2015, **25**, 812–820.
- 24 N. A. Usov, M. S. Nesmeyanov and V. P. Tarasov, *Sci. Rep.*, 2018, **8**, 1224.
- 25 H. Gao, T. Zhang, Y. Zhang, Y. Chen, B. Liu, J. Wu, X. Liu, Y. Li, M. Peng, Y. Zhang, G. Xie, F. Zhao and H. M. Fan, *J. Mater. Chem. B*, 2020, **8**, 515–522.
- 26 W. L. Gan, M. Chandra Sekhar, D. W. Wong, I. Purnama, S. Y. Chiam, L. M. Wong and W. S. Lew, *Appl. Phys. Lett.*, 2014, **105**, 152405.
- 27 W. Wong, W. L. Gan, Y. K. Teo and W. S. Lew, *Nanoscale Res. Lett.*, 2019, **14**, 376.
- 28 M. Kim, X. Xu, R. Xin, J. Earnshaw, A. Ashok, J. Kim, T. Park, A. K. Nanjundan, W. A. El-Said, J. W. Yi, J. Na and Y. Yamauchi, *ACS Appl. Mater. Interfaces*, 2021, **13**, 52034–52043.
- 29 M. Kim, K. L. Firestein, J. F. S. Fernando, X. Xu, H. Lim, D. V. Golberg, J. Na, J. Kim, H. Nara, J. Tang and Y. Yamauchi, *Chem. Sci.*, 2022, **13**, 10836–10845.
- 30 M. Kim, C. Wang, J. Earnshaw, T. Park, N. Amirilian, A. Ashok, J. Na, M. Han, A. E. Rowan, J. Li, J. W. Yi and Y. Yamauchi, *J. Mater. Chem. A*, 2022, **10**, 24056–24063.
- 31 M. Mandal Goswami, *Sci. Rep.*, 2016, **6**, 35721.
- 32 S. Liu, K. Dou, B. Liu, M. Pang, P. Ma and J. Lin, *Angew. Chem., Int. Ed.*, 2023, **62**, e202301831.
- 33 D. Zhao, Y. Wei, J. Xiong, C. Gao and D. Wang, *Adv. Funct. Mater.*, 2023, **33**, 2300681.
- 34 S. Ganguly and S. Margel, *Prog. Polym. Sci.*, 2022, **131**, 101574.
- 35 F. H. Aragon, J. A. Coaquira, L. Villegas-Lelovsky, S. W. da Silva, D. F. Cesar, L. C. Nagamine, R. Cohen, E. Menendez-Proupin and P. C. Morais, *J. Phys.: Condens. Matter*, 2015, **27**, 095301.
- 36 F. Nakagomi, P. E. N. de Souza, T. J. Castro, V. K. Garg, A. C. Oliveira, F. C. E. Silva, A. Franco, P. C. Morais and S. W. da Silva, *J. Alloys Compd.*, 2020, **842**, 155751.
- 37 I. S. B. Ferraz, T. J. Castro, J. Mantilla, J. A. H. Coaquira, V. K. Garg, A. C. Oliveira, A. Franco, P. C. Morais and S. W. da Silva, *J. Alloys Compd.*, 2021, **887**, 161398.
- 38 G. Padmapriya, A. Manikandan, V. Krishnasamy, S. K. Jaganathan and S. A. Antony, *J. Supercond. Novel Magn.*, 2016, **29**, 2141–2149.
- 39 M. Li, H. Fang, H. Li, Y. Zhao, T. Li, H. Pang, J. Tang and X. Liu, *J. Supercond. Novel Magn.*, 2017, **30**, 2275–2281.
- 40 T. Nie, S. Cao, Y. Wang, Z. Ji, Z. Bai, J. Yan and X. Yan, *Energy Technol.*, 2021, **9**, 2100249.
- 41 E. R. L. Siqueira, W. O. Pinheiro, V. R. R. Aquino, B. C. P. Coelho, A. F. Bakuzis, R. B. Azevedo, M. H. Sousa and P. C. Morais, *Nanomaterials*, 2022, **12**, 2760.
- 42 V. R. R. Aquino, J. C. R. Aquino, J. A. H. Coaquira, A. F. Bakuzis, M. H. Sousa and P. C. Morais, *Mater. Des.*, 2023, **232**, 112082.
- 43 K. Shen, Y. Yan, Z. Xue, S. Wu, J. You, L. Li and W. S. Lew, *ACS Appl. Nano Mater.*, 2023, **6**, 13330–13341.
- 44 P. C. Morais and D. C. Silva, *Nanomaterials*, 2022, **12**, 413.
- 45 Z. Li, D. Wang, M. Xu, J. Wang, X. Hu, S. Anwar, A. C. Tedesco, P. C. Morais and H. Bi, *J. Mater. Chem. B*, 2020, **8**, 2598–2606.
- 46 Y. Wang, S. Luo, Y. Wu, P. Tang, J. Liu, Z. Liu, S. Shen, H. Ren and D. Wu, *ACS Nano*, 2020, **14**, 17046–17062.
- 47 N. Liu, L. Wu, W. Zuo, Q. Lin, J. Liu, Q. Jin, Z. Xiao, L. Chen, Y. Zhao, J. Zhou and X. Zhu, *ACS Appl. Mater. Interfaces*, 2022, **14**, 29668–29678.